RF-ECG: Heart Rate Variability Assessment Based on COTS RFID Tag Array

CHUYU WANG, Nanjing University, CHN
LEI XIE*, Nanjing University, CHN
WEI WANG, Nanjing University, CHN
YINGYING CHEN, Rutgers University, USA
YANLING BU, Nanjing University, CHN
SANGLU LU, Nanjing University, CHN

As an important indicator of autonomic regulation for circulatory function, Heart Rate Variability (HRV) is widely used for general health evaluation. Apart from using dedicated devices (e.g, ECG) in a wired manner, current methods search for a ubiquitous manner by either using wearable devices, which suffer from low accuracy and limited battery life, or applying wireless techniques (e.g., FMCW), which usually utilize dedicated devices (e.g., USRP) for the measurement. To address these issues, we present RF-ECG based on Commercial-Off-The-Shelf (COTS) RFID, a wireless approach to sense the human heartbeat through an RFID tag array attached on the chest area in the clothes. In particular, as the RFID reader continuously interrogates the tag array, two main effects are captured by the tag array: the *reflection effect* representing the RF-signal reflected from the heart movement due to heartbeat; the *moving effect* representing the tag movement caused by chest movement due to respiration. To extract the reflection signal from the noisy RF-signals, we develop a mechanism to capture the RF-signal variation of the tag array caused by the *moving effect*, aiming to eliminate the signals related to respiration. To estimate the HRV from the reflection signal, we propose a signal reflection model to depict the relationship between the RF-signal variation from the tag array and the *reflection effect* associated with the heartbeat. A fusing technique is developed to combine multiple reflection signals from the tag array for accurate estimation of HRV. Experiments with 15 volunteers show that RF-ECG can achieve a median error of 3% of Inter-Beat Interval (IBI), which is comparable to existing wired techniques.

CCS Concepts: • **Networks** → Sensor networks; **Mobile networks**; • **Human-centered computing** → **Mobile devices**;

Additional Key Words and Phrases: RFID; Heart rate; HRV

ACM Reference Format:
Chuyu Wang, Lei Xie, Wei Wang, Yingying Chen, Yanling Bu, and Sanglu Lu. 2018. RF-ECG: Heart Rate Variability Assessment Based on COTS RFID Tag Array. *Proc. ACM Interact. Mob. Wearable Ubiquitous Technol.* 2, 2, Article 85 (June 2018), 26 pages. https://doi.org/10.1145/3214288

*Lei Xie is the corresponding author, Email: lxie@nju.edu.cn.

Authors' addresses: Chuyu Wang, wangcyu217@dislab.nju.edu.cn, Nanjing University, State Key Laboratory for Novel Software Technology, 163 Xianlin Ave, Nanjing, 210046, CHN; Lei Xie, lxie@nju.edu.cn, Nanjing University, State Key Laboratory for Novel Software Technology, 163 Xianlin Ave, Nanjing, 210046, CHN; Wei Wang, Nanjing University, State Key Laboratory for Novel Software Technology, 163 Xianlin Ave, Nanjing, 210046, CHN; Yingying Chen, Rutgers University, WINLAB, North Brunswick, NJ, 08902, USA; Yanling Bu, Nanjing University, State Key Laboratory for Novel Software Technology, 163 Xianlin Ave, Nanjing, 210046, CHN; Sanglu Lu, Nanjing University, State Key Laboratory for Novel Software Technology, 163 Xianlin Ave, Nanjing, 210046, CHN.

2474-9567/2018/6-ART85 $15.00
https://doi.org/10.1145/3214288

1 INTRODUCTION

1.1 Motivation

Heart Rate Variability (HRV) represents the variation of the time interval between adjacent heartbeats [7]. As an important indicator of autonomic regulation for circulatory function, HRV reflects how the cardiovascular regulatory system responds to demands, stress and illness [35]. Fine-grained HRV information is usually important to quantitatively measure physiological and mental changes during treatment. For example, the frequent detection of the premature beats indicates some kinds of heart problems about the person. Currently, reduced HRV has been used as a marker of aging, decreased autonomic activity, diabetic neuropathy, and increased risk of sudden cardiac death. According to the news from WHO [2], more than 17 million people die annually from cardiovascular disease (CVD), an estimated 31% of all deaths worldwide. Efficient HRV assessment can not only provide accurate information about the heart states for the treatment of heart diseases and the adjustment of mental status, but also timely detect the heart problem in the early stage. Therefore, accurate and fine-grained HRV assessment is regarded as one of the most effective methods for the general health evaluation [29].

1.2 Limitation of Prior Art

HRV analysis is normally based on the Inter-Beat Interval (IBI) measurements, which accurately describes the time interval between the adjacent heartbeats. As a traditional approach, the electrocardiogram (ECG) is regarded as the standard way to measure the IBI [6], which can accurately measure the IBI information from the tiny electrical changes on the skin. But the user is usually tethered to the electrodes in a wired manner, which imposes restrictions on the range of daily activities of the user. Moreover, it requires direct skin contact, indicating some people need to remove the chest hair to achieve better signal quality. Some optical absorption methods leverages the photoplethysmograph (PPG) [12, 18] to estimate the IBI information. But it usually relies on the reflection of infrared light, leading to the loss of waveform detail and time accuracy. Commercial devices (*e.g.*, wristbands [5]) try to integrate the sensors (electrodes or visual sensors) into fabrics for wearable applications. However, they are only designed to estimate the average heart rate within a duration, which works as a training aid for exercises. So the fine-grained heart problems, such as premature beats and heart arrhythmia, cannot be effectively detected, which requires the accurate estimation of the IBI information. Moreover, these wearable devices are mostly constrained by their limited battery life, requiring frequent battery recharging. This limits the efficient HRV monitoring for elderly people and infants, who may forget to recharge the wearable devices. To eliminate the dependency on such sensing devices, a number of device-free methods are proposed to perceive the heartbeat via wireless channel (e.g., Wi-Fi and FMCW) [10, 11, 42]. However, they usually depend on the dedicated devices

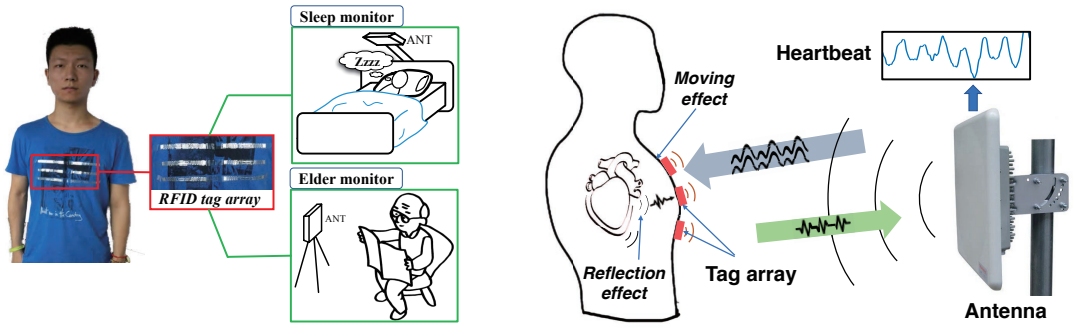

(a) Illustrations of applications of RF-ECG

(b) Illustration of working flow of RF-ECG

Fig. 1. RF-ECG system scenario.

(e.g., USRP [10] and RFID with conductive fabric electrodes [11]), and thus are expensive compared with the commercial devices. Additionally, some professional skills are required to operate the dedicated devices, which is not suitable for applications in a ubiquitous environment. Moreover, when multiple people are within the sensing range, the device-free property prevents them from effectively distinguishing multiple human subjects and performing HRV monitoring simultaneously. Therefore, a new solution based on Commercial-off-the-Shelf (COTS) devices is desirable to the above limitations in a *lightweight* and *distinguishable* approach.

1.3 Our Approach

The emerging RFID technology [15, 25, 27, 34, 37, 38, 40] has brought new opportunities for HRV monitoring in a more convenient and accurate approach, as the RFID tag can be regarded as an extremely lightweight sensor and its nature of identification can be used to effectively and easily distinguish different human subjects. In this paper, we propose RF-ECG, an RFID-based approach to perform HRV monitoring on human subjects, which aims to recover the IBI information with a similar accuracy as the traditional ECG based on the COTS RFID devices. Specifically, instead of designing a dedicated platform [11], we attach a set of COTS RFID tags on the chest area in the clothes of the human subject, which forms a tag array for comprehensive sensing. We deploy a COTS RFID reader to continuously interrogate these tags by issuing a *continuous wave*, and collect their *backscattered RF-signals* within the effective scanning range ($1 \sim 3$m). Similarly to the traditional ECG-based approaches, we focus on the HRV monitoring with a relatively quite environment, where the users are supposed to keep still during the measurement. Figure 1(a) illustrates the deployment of tag array of RF-ECG, where 6 tags form a 2×3 tag array. Through the RF-signal from the tag array, RF-ECG is able to facilitate two main applications for HRV monitoring in daily life. Firstly, by deploying the antenna above the bed, RF-ECG is able to monitor the user's heart status during sleeping, which can further enable the treatment of sleep apnea [1] and sleep stage detection [21]. Such mode can be extended to infant monitoring, because infants spend most of the time sleeping in the cribs. Secondly, since elderly people are usually less active and spend lots of time in performing more stationary activities (*e.g.*, watching TVs), we can deploy the antenna in the living room and bedroom for efficient HRV monitoring. Such HRV monitoring can offer rapid and effective diagnostic clues for the general health evaluation. Toward these monitoring applications, Figure 1(b) further presents the diagram of our HRV monitoring approach. As the heart beats behind the human chest, the *continuous wave* reflected from the heart movement could be captured by the tag array, and then backscattered to the RFID reader via the *RF-signals* [41], which we call the *reflection effect* of the tag array. Meanwhile, the *RF-signals* are also affected by the chest movements due to human respiration, which we call the *moving effect* of the tag array. Hence, the RF-signals received by the RFID reader consist of *heartbeat signal*, *respiration signal* and the ambient noise from the environment. In this paper, we investigate the possibility of extracting such tiny reflection signals corresponding to the heartbeat, while eliminating other signal interferences from the human respiration and the ambient noise in the multi-path environment. In particular, according to the RF-signals received from the tag array, we develop a mechanism to capture the chest movement, aiming to cancel the *respiration signal* corresponding to the *moving effect*. Then, by using the wavelet-based signal denoising, we further extract the *heartbeat signals* corresponding to the *reflection effect*. Finally, we build a model to depict the *reflection effect* on RF-signals of different tags from the tag array, and extract the Inter-Beat Interval (IBI) for HRV monitoring.

1.4 Challenges

There are three main challenges in performing the HRV assessment via the RFID based approach. The first challenge is to detect and extract weak heartbeat signals from RFID tags among multiple interferences caused by human respiration and ambient noises. In particular, the signal variation captured by the reflection effect from heartbeat is much weaker than the signal variation caused by the moving effect from respiration. To address

this challenge, we develop a mechanism to depict the RF-signal variation of the tag array caused by the chest movement, helping to eliminate the part of the respiration signals corresponding to the moving effect. We further build a model to depict the reflection effect on RF-signals of different tags from the tag array. By fusing the RF-signals from multiple tags, we are able to strengthen the heartbeat signals while suppressing the signal interferences from the others.

The second challenge is to achieve a fine-grained heart beat estimation for the HRV assessment according to the reflection effect. Instead of simply calculating the heart rate, which could be estimated through the Fast Fourier Transform results, the fine-grained HRV assessment requires to estimate the beat-to-beat interval by performing accurate beat segmentation. To address this challenge, after eliminating the respiration signals, we apply the wavelet-based denoising method to further filter out the ambient noise signals outside the frequency band of heart rate. The filtered signals thus can show a clear periodic pattern to facilitate fine-grained IBI segmentation. Finally, we propose a PCA-based scheme to derive a template to depict the inter-beat signals and use it to iteratively perform the IBI segmentation.

The third challenge is to understand the sensing mechanism of RFID tag array and leverage the RFID tag array to perform accurate sensing on HRV. Specifically, as multiple tags are deployed on the human body, these tags can be regarded as a *non-rigid body array* to perceive the *moving effect*, since the tags may have relative displacement during the process of respiration; they can also be regarded as a *rigid body array* to perceive the *reflection effect*, after eliminating the respiration signal from the received RF-signal. To fuse multiple RF-signals from the tag array for accurate sensing, we capture the relationship between the RF-signals from the tag array and the corresponding movement from the heartbeat or respiration, via our reflection effect model and the moving effect mechanism, respectively. Based on the above techniques, we are able to perform data fusion over RF-signals from the RFID tag array for accurate sensing on HRV.

1.5 Contributions

This paper makes four contributions: First, to the best of our knowledge, this is the first work that investigates the feasibility of Heart Rate Variability assessment based only on the COTS RFID. We leverage the RFID tag array to perform accurate sensing on HRV assessment in a lightweight and distinguishable approach. Second, we have conducted in-depth investigation on the sensing mechanism of RFID tag array. We develop a reflection effect model and a moving effect mechanism, respectively, to capture the relationship between the RF-signals from the tag array and the corresponding movement from the heart beat or respiration. Third, we design novel algorithms to extract the HRV from the RF-signals mixed with heartbeat signals, respiration signals, and ambient noises. We use wavelet-based signal denoising and signal fusion from tag array to remove the interferences to extract the IBI from the heartbeat signals. Fourth, we implement a system prototype for HRV assessment in the practical environment, and evaluate the performance with extensive experiments. Experiment results show that RF-ECG can achieve a median IBI error of 24ms, i.e., about 3% error of a normal IBI value, which is compatible to existing wired techniques.

2 RELATED WORK

Sensor-based heartbeat detection: Photoplethysmogram (PPG) sensors are widely used for heart rate estimation by using a pulse oximeter, which illuminates the skin and measures the changes in light absorption [8]. Current wearable devices (e.g., smartwatches and fitness trackers [3–5]) usually use the PPG-based technology to measure the heart rate. However, body motion can easily distort the waveform of PPG, which causes large noise for heart rate sensing. To address this issue, recent research employs the inertial measurement units (IMU) to improve the overall accuracy of PPG [12, 18]. Besides PPG, Zou *et al.* develop a heart rate monitoring system using nanofiber-based strain sensors, which could be more compliant and comfortable [43]. However, these

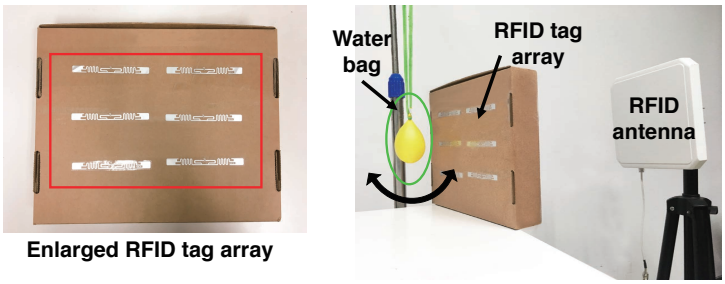

Fig. 2. Empirical study setup.

dedicated sensors are fairly expensive and battery-hungry, so it is not suitable for large-scale usage and long-term deployment. HB-phone [22] estimates the human heart rate based on the vibration sensors mounted on the bed, which provides the heartbeat monitoring during sleeping. However, it only provides the average heart rate during a time window without the fine-grained IBI information. Recently, researchers try to measure the heart rate by using the smartphone cameras [19, 24, 31], which require the user to place her fingertip on the camera. Such vision-based approaches heavily rely on the user's pose as well as the illumination condition; moreover, as the signals are collected from the weak pulse, the accuracy is relatively lower than the approaches of obtaining the signals directly from the heartbeat. In contrast, our solution measures the heartbeat using the signal reflected from the heart, which could be more accurate than the pulse-based measurement. In addition, our solution leverages the battery-free RFID tags for heartbeat detection, which is more lightweight, scalable and not limited by the battery life.

RF-based heartbeat detection: Recent research has shown that RF-signals are sensitive to the changes of the multi-path environments [9, 14, 23, 39, 41], thus both the heartbeat and breathing can be detected according to the variation of the RF-signals without requiring the user to hold or wear any device. Radar-based approaches, such as FMCW [10, 42], doppler radar [17, 29], are accurate at measuring such tiny environmental changes. However, they usually require dedicated hardware and incur high cost for daily heartbeat monitoring. Nguyen *et al.* [30] try to estimate the respiration rate and heart rate based on a radio transceiver and a radar navigator. But it requires specific motion devices for navigation, and it only provides the coarse-grained heart rate estimation. Wi-Fi based approaches focus on estimating the vital signs using commercial off-the-shelf (COTS) Wi-Fi devices. Specifically, they mainly leverage the Channel State Information (CSI) from both the time and frequency domain to estimate the breathing rate and heart rate [26, 28, 36]. However, both the radar and Wi-Fi based techniques cannot label the subject, due to their device free characteristic. Therefore, it is difficult to distinguish and monitor multiple users simultaneously, especially when users share similar breathing or heartbeat patterns. To address this problem, Adib *et al.* proposed a radar technique to monitor the vital signs of multiple people simultaneously, by separating reflectors into different buckets depending on the distance between these people and the device [10]. Hence, it requires the human subjects to be separated with a considerable distance for efficient distinction. In contrast to the previous work, in this paper, we propose a novel approach for heartbeat sensing via RFID tag array, which can be regarded as an extremely lightweight sensor. Moreover, its nature of identification can be used to effectively distinguish multiple human subjects, even if these human subjects are very close to each other.

3 UNDERSTANDING HEART RATE VARIABILITY

3.1 Measurement of Periodic Signal via RFID Tag Array

In order to systematically study how to use an RFID tag array to passively sense a periodic signal, e.g., the heartbeat signal, we first use a controlled experiment to investigate the *reflection influence* of the periodic signal on the tag array, which is reflected from a signal source without attaching an RFID tag. Specifically, we manually

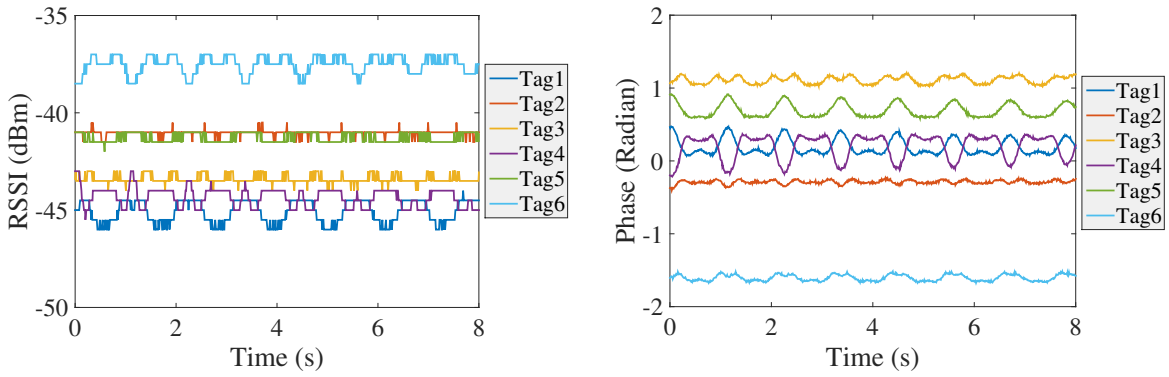

(a) RSSI trend in bag swing

(b) Phase trend in bag swing

Fig. 3. Preliminary study: Measurement of periodic signal on the RFID tag array.

generate a periodic signal source by swinging a water bag as a plummet and sense the period of the water bag from a pre-deployed tag array. As shown in Figure 2, we hang a water bag to emulate the periodic signal and investigate the signal changes as we swing the water bag. A 2×3 tag array is deployed on the surface of a box, which is $10cm$ away from the water bag, to sense the periodic signal of the water bag. The size of the tag array is designed based on the size of human chest, so that the same tag array can be deployed on the chest area in the clothes of the human subject. An RFID antenna is deployed $2m$ away from the tag array to continuously interrogate the tags on the array.

We observe that both the phase and RSSI waves have clear periodic patterns during the swing process of the water bag, but the periodic shapes are different from each tag. In particular, we swing the water bag as a pendulum to generate the periodic signal. The length of the pendulum is $25cm$ so that the period is about $1Hz$ in our setup. We show both the RSSI and phase trend of the selected tags from the tag array, respectively, in Figure 3(a) and Figure 3(b). We can clearly observe the periodical pattern in the waves of RSSI and phase trend during the swing process of water bag. The reason is that, the swing periodically changes the position of the reflection surface, thus the propagation paths (i.e., multi-path effect) of the RF-signal are changed as well, which further leads to the periodical variation in the RF-signals. In regard to the difference of the absolute RSSI value, it is caused by the different positions of each tag. Moreover, even if all the tags present the same cycle time, the exact shape of their waveforms are different among the tags. This indicates that different tags on the tag array have different sensitivities to the reflection effect of the swing bag. We will build a theoretical model to explain the phenomenon later in Section 3.3.

3.2 Measurement of HRV in Real Settings

We further investigate how the actual heartbeat affects the RF-signals in real settings. Specifically, we attach a 2×3 tag array on the chest area in the clothes of the human subject. We first let the human subject hold the breath for 20s, indicating that the chest movement of breathing can be negligible. We then let the human subject breathe normally for 20s, and thus there exists obvious chest movement of breathing. We respectively collect the phase/RSSI values of these two sets. We select an arbitrary tag from the tag array and present the results in Figure 4.

According to Figure 4(a), we can observe weak but fairly clear periodic heartbeat patterns from the phase sequences, since the chest movement of breathing can be negligible. According to Figure 4(b), we can observe obvious periodic respiration patterns for the chest movement of breathing, as the *moving effect* due to the chest movement clearly changes the phase values. However, the periodic heartbeat patterns can hardly be detected

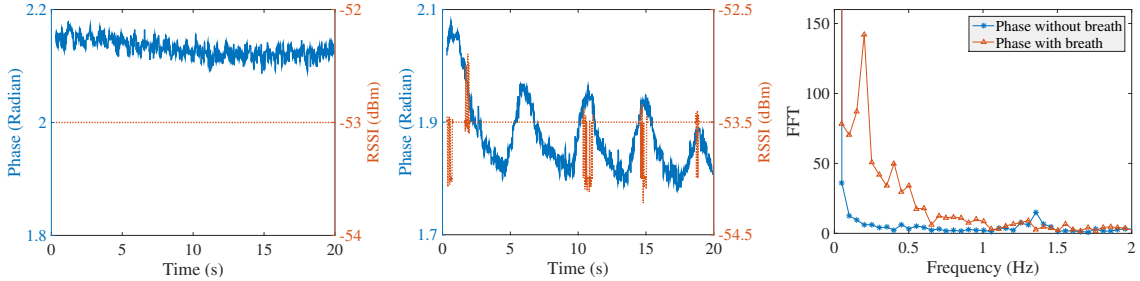

(a) The phase/RSSI sequence without breathing (b) The phase/RSSI sequence with breathing (c) Frequency domain analysis of the phase sequence

Fig. 4. Preliminary study: measurement of HRV with and without breathing.

anymore, since the *reflection effect* is orders of magnitude smaller than the *moving effect* in the tag array. Besides, we cannot detect any periodic patterns from the RSSI sequences in both situations, since the resolution of RSSI is rather coarse-grained. We further perform *FFT analysis* on the phase sequences from the frequency domain. Figure 4(c) shows the experiment results in both situations. For the situation without breathing, we can clearly find a small peak at $1.355Hz$, which is corresponding to the heartbeat frequency band. This asserts the reflection effect exists but relatively small. For the situation with breathing, we can clearly detect a peak at $0.2Hz$, which corresponds to the respiration frequency band, besides, we can only detect a very small peak at $1.3Hz$, which is almost buried in the noises. Therefore, to obtain the precise heartbeat signal, it is essential to first remove the influence of respiration and then strengthen the heartbeat reflection.

3.3 Modeling HRV via Tag Array Sensing

In this subsection, we model the relationship between the RF-signals from the tag array and the heart displacement in the reflection effect, which is the periodic signal of the heartbeat.

3.3.1 Extracting the Reflection Signal. To understand how the *heart displacement* affects the reflection effect, it is essential to extract the reflection signal from the received RF-signal, i.e., the RF-signal reflected from the heart to the tags. Hence, we use a signal propagation model to depict the RF-signal transmission with the reflection effect. As shown in Figure 5, we use $\mathcal{A}$, $\mathcal{T}$, $\mathcal{B}$ and $\mathcal{C}$ to denote the RFID antenna, RFID tag, reflection object and background environment, respectively. First, the antenna $\mathcal{A}$ sends the continuous wave to activate the tags. Due to the multi-path effect, the tag $\mathcal{T}$ receives a superposed signal, which contains the line-of-sight (LOS) signal $S_{\mathcal{A}\to\mathcal{T}}$ (blue line), the *reflection signal* $S_{\mathcal{A}\to\mathcal{B}\to\mathcal{T}}$ from the reflection object $\mathcal{B}$ (red line), as well as the reflection signal $S_{\mathcal{A}\to\mathcal{C}\to\mathcal{T}}$ from the background environment (green line). Then, after the specified tag is successfully activated, it backscatters the signal to the antenna with necessary data modulation. Hence, the *raw signal* received by the antenna $\mathcal{A}$ can be represented as:

$$S_r = h_{\mathcal{T}\to\mathcal{A}} h_{\mathcal{T}} (S_{\mathcal{A}\to\mathcal{T}} + S_{\mathcal{A}\to\mathcal{B}\to\mathcal{T}} + S_{\mathcal{A}\to\mathcal{C}\to\mathcal{T}}), \tag{1}$$

where $h_{\mathcal{T}\to\mathcal{A}}$ represents the signal attenuation due to propagation path loss and $h_{\mathcal{T}}$ is the reflection coefficient of the tag. Since both the LOS signal and the reflection signal from the background environment are usually stable during the whole propagation, we combine them as

$$S_{r,0} = h_{\mathcal{T}\to\mathcal{A}} h_{\mathcal{T}} (S_{\mathcal{A}\to\mathcal{T}} + S_{\mathcal{A}\to\mathcal{C}\to\mathcal{T}}), \tag{2}$$

and denote the remained reflection signal from the reflection object as

$$S_{r,1} = h_{\mathcal{T}\to\mathcal{A}} h_{\mathcal{T}} S_{\mathcal{A}\to\mathcal{B}\to\mathcal{T}}. \tag{3}$$

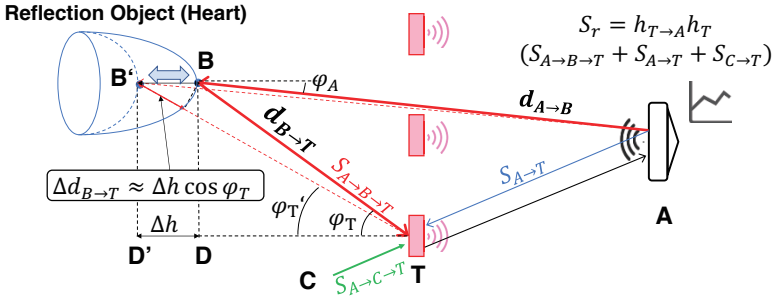

Fig. 5. Reflection model of heart displacement.

To extract the reflection signal $S_{r,1}$ from the superposed signal S_r, we could subtract the complex signal $S_{r,0}$ [41], which can be measured simply by removing the reflection object.

Figure 6 shows the RSSI and phase variation of the reflection signals from periodic signal of the water bag according to the subtraction $S_{r,1} = S_r - S_{r,0}$. We note that, for each reflection signal, the RSSI variation is irregular and its value is usually less than $-60dBm$, as the power of the reflection signal is rather weak and easy to be affected. In fact, since the reflection object, i.e., the water bag, only moves a small distance, theoretically the RSSI variation should be very small according to Friis Equation [16]. Meanwhile, the phases of the reflection signal from different tags all have obvious periodical patterns in the waveforms. Moreover, they not only have some similarities in the waveform contours, but also have differences in the waveform details among each other. Therefore, this implies that all the tags are subjected to similar reflection influence, but the performance in sensitivity are different among different tags.

3.3.2 Estimating Heart Displacement via a Single Tag. After extracting the reflection signal, it is essential to further figure out the relationship between the heart displacement and the reflection RF-signal. Since the phase of reflection signal is more sensitive to the heart displacement than RSSI, we use the phase as a metric for RF-signal to depict the corresponding relationship. According to Eq.(3), let λ be the wave length of RF-signal, the phase of reflection signal $S_{r,1}$ can be calculated from the reflection path length as:

$$\theta^r_{\mathcal{T}} = 2\pi\left(\frac{d_{\mathcal{T}\to\mathcal{A}} + d_{\mathcal{A}\to\mathcal{B}} + d_{\mathcal{B}\to\mathcal{T}}}{\lambda} + \theta_{cons}\right) \mod 2\pi, \tag{4}$$

where the superscript ^{r} indicates the reflection signal and θ_{cons} is the constant phase deviation due to reflection. Since $d_{\mathcal{T}\to\mathcal{A}}$ is fixed during the whole propagation and θ_{cons} is constant, when the reflection object moves from $\mathcal{B}$ to $\mathcal{B}'$, the phase change $\Delta\theta^r_{\mathcal{T}}$ only depends on the change of path length $\Delta d_{\mathcal{A}\to\mathcal{B}}$ and $\Delta d_{\mathcal{B}\to\mathcal{T}}$, as:

$$\Delta\theta^r_{\mathcal{T}} = 2\pi\frac{\Delta d_{\mathcal{A}\to\mathcal{B}} + \Delta d_{\mathcal{B}\to\mathcal{T}}}{\lambda} \mod 2\pi. \tag{5}$$

Without loss of generality, we first consider the path length change $\Delta d_{\mathcal{B}\to\mathcal{T}}$. Assume that the points $\mathcal{D}$ and $\mathcal{D}'$ are respectively the projection of the points $\mathcal{B}$ and $\mathcal{B}'$ on the horizontal line of $\mathcal{T}$ in Figure 5, then the edge length $d_{\mathcal{B}\mathcal{D}} = d_{\mathcal{B}'\mathcal{D}'}$. When the reflection object moves from $\mathcal{B}$ to $\mathcal{B}'$, the reflection path changes from $d_{\mathcal{B}\to\mathcal{T}}$ to $d_{\mathcal{B}'\to\mathcal{T}}$, which are, respectively, the hypotenuses of two right triangles $\triangle\mathcal{B}\mathcal{D}\mathcal{T}$ and $\triangle\mathcal{B}'\mathcal{D}'\mathcal{T}$. Let $\phi_{\mathcal{T}}$ and $\phi'_{\mathcal{T}}$ to denote the angle $\angle\mathcal{B}\mathcal{T}\mathcal{D}$ and $\angle\mathcal{B}'\mathcal{T}\mathcal{D}'$, respectively. Then, the path length change $\Delta d_{\mathcal{B}\to\mathcal{T}}$ can be calculated as follows:

$$\Delta d_{\mathcal{B}\to\mathcal{T}} = d_{\mathcal{B}'\mathcal{T}} - d_{\mathcal{B}\mathcal{T}} = \frac{d_{\mathcal{B}\mathcal{D}}}{\sin\phi'_{\mathcal{T}}} - \frac{d_{\mathcal{B}\mathcal{D}}}{\sin\phi_{\mathcal{T}}}. \tag{6}$$

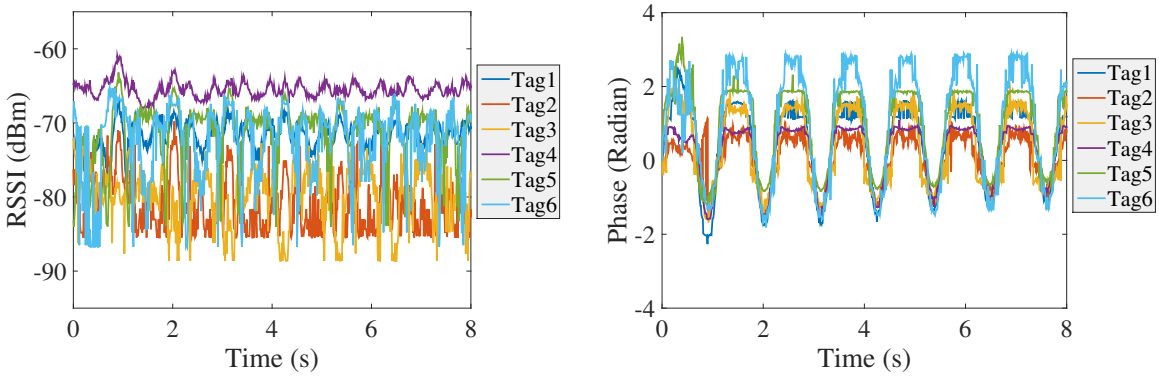

(a) The RSSI of the reflection signal

(b) The phase of the reflection signal

Fig. 6. The extracted reflection signal.

Let Δh be the displacement of the reflection object (i.e., the heart displacement $d_{\mathcal{B}'\mathcal{B}}$), it is essentially equal to

$$\Delta h = d_{\mathcal{B}'\mathcal{B}} = d_{\mathcal{D}'\mathcal{D}} = \frac{d_{\mathcal{B}\mathcal{D}}}{\tan\phi'_{\mathcal{T}}} - \frac{d_{\mathcal{B}\mathcal{D}}}{\tan\phi_{\mathcal{T}}}. \tag{7}$$

By combining the two equations to remove $d_{\mathcal{B}\mathcal{D}}$, we obtain

$$\Delta d_{\mathcal{B}\to\mathcal{T}} = \Delta h \frac{\sin\phi_{\mathcal{T}} - \sin\phi'_{\mathcal{T}}}{\sin(\phi_{\mathcal{T}} - \phi'_{\mathcal{T}})}. \tag{8}$$

If we define the angle deviation $\Delta\phi_{\mathcal{T}} = \phi_{\mathcal{T}} - \phi'_{\mathcal{T}}$, then $\phi'_{\mathcal{T}} = \phi_{\mathcal{T}} - \Delta\phi_{\mathcal{T}}$, thus

$$\Delta d_{\mathcal{B}\to\mathcal{T}} = \Delta h(\cos\phi_{\mathcal{T}} + \sin\phi_{\mathcal{T}} \frac{1-\cos\Delta\phi_{\mathcal{T}}}{\sin\Delta\phi_{\mathcal{T}}}). \tag{9}$$

In regard to the heartbeat, the reflection object (i.e., the heart) actually moves a rather small distance Δh, thus the angle deviation $\Delta\phi_{\mathcal{T}} \to 0$. Hence, $\frac{1-\cos\Delta\phi_{\mathcal{T}}}{\sin\Delta\phi_{\mathcal{T}}} = \tan\frac{\Delta\phi_{\mathcal{T}}}{2} \to 0$. Therefore, Eq (9) can be simplified as follows:

$$\Delta d_{\mathcal{B}\to\mathcal{T}} \approx \Delta h\cos\phi_{\mathcal{T}}. \tag{10}$$

Similarly, for the path length change $\Delta d_{\mathcal{A}\to\mathcal{B}}$, let $\phi_{\mathcal{A}}$ denote the angle between $\mathcal{AB}$ and the horizontal line, we also obtain $\Delta d_{\mathcal{A}\to\mathcal{B}} \approx \Delta h\cos\phi_{\mathcal{A}}$.

Therefore, by combining Eq. (10) and Eq. (5), we obtain

$$\Delta\theta^r_{\mathcal{T}} \approx \frac{2\pi\Delta h(\cos\phi_{\mathcal{T}} + \cos\phi_{\mathcal{A}})}{\lambda} \mod 2\pi. \tag{11}$$

Hence, for any arbitrary tag T, given the phase change of the reflection signal $\Delta\theta^r_{\mathcal{T}}$, the heart displacement Δh can be estimated as follows:

$$\Delta h \approx \frac{(\Delta\theta^r_{\mathcal{T}} + 2\pi k)\lambda}{2\pi(\cos\phi_{\mathcal{T}} + \cos\phi_{\mathcal{A}})}, \ \textit{where}\ k = \cdots, -1, 0, 1, \cdots \tag{12}$$

Here, k represents the periods of the phase values. Since the heart displacement is rather small, k equals to 0 in our problem.

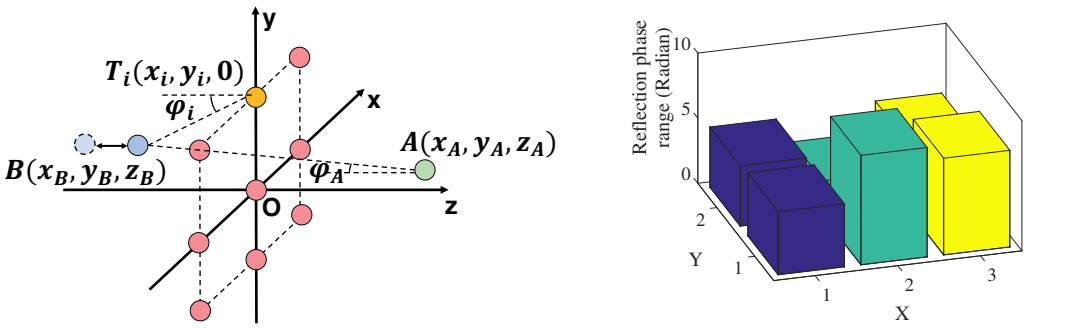

(a) Compute the parameters $\cos\phi_i$ and $\cos\phi_{\mathcal{A}}$ in the 3D coordinate system

(b) The phase change of reflection signal for different tags

Fig. 7. Heart displacement estimation via tag array.

3.3.3 Estimating Heart Displacement via Tag Array. In Section 3.3.2, we derive the relationship between the heart displacement and the reflection signal from a single tag, according to the model in Eq.(12). However, due to the issues such as the multi-path effect and the ambient noises, the reflection signal from a single tag can be distorted if it is deployed in a position with interferences and noises, which further leads to the errors in the heart displacement estimation. Therefore, it is essential to further investigate the reflection signals of multiple tags from different positions of the tag array to improve the sensing performance.

Suppose we build a 3-dimensional coordinate system by setting the center of the tag array as the origin O, the X and Y-axis are parallel to the tag array, whereas the Z-axis is orthogonal to the tag array. Then, each tag T_i from the tag array can be denoted as a point with the coordinate $(x_i, y_i, 0)$. Assume that the reflection object (e.g., the heart) can be regarded as a virtual point B according to the overall reflection effect, thus it can be denoted with the coordinate (x_B, y_B, z_B). Besides, the antenna $\mathcal{A}$ can be denoted with the coordinate (x_A, y_A, z_A). Then, as shown in Figure 7(a), for an arbitrary tag $\mathcal{T}_i$ from the tag array, the parameters $\cos\phi_i$ (i.e., $\cos\phi_{\mathcal{T}}$ for tag $\mathcal{T}_i$) and $\cos\phi_{\mathcal{A}}$ from the model in Eq.(12) can be depicted as follows:

$$\begin{cases} \cos\phi_i = \dfrac{|z_B|}{\sqrt{(x_B - x_i)^2 + (y_B - y_i)^2 + z_B^2}} \\ \cos\phi_{\mathcal{A}} = \dfrac{|z_B - z_A|}{\sqrt{(x_B - x_A)^2 + (y_B - y_A)^2 + (z_B - z_A)^2}} \end{cases} \tag{13}$$

According to the model of phase change in Eq.(11), in regard to different tags from the tag array, the parameter $\phi_{\mathcal{A}}$ is only related to the reflection object, so it should be consistent for all tags; the parameter ϕ_i actually depends on the exact position of the tag $\mathcal{T}_i$, so it should be different for different tags. According to Eq.(11), the smaller the value of ϕ_i is, the larger phase change of the tag $\mathcal{T}_i$ is obtained. This implies that the reflection object causes larger signal influences to the tags which is more close in position. Based on this property, it is possible to further locate the position of the reflection object (i.e., the heart), according to the signal variances from the tag array.

We further validate this hypothesis with an empirical study. The experiment setup is the same as Section 3.1. We deploy a 2×3 tag array to detect the reflection of the swinging water bag, and label each tag as (x, y) according to its order in the specified dimension. The center of the water bag is located around the coordinate $(2.5, 1.5)$. We show the reflection phase range of all the 6 tags in Figure 7(b). It is found that the tag at $(2, 1)$ has the largest reflection phase range, whereas the other tags gradually decreases, as they are away from the tag at $(2, 1)$. Moreover, based on the amplitude of the reflection phase, we can infer the position of the water bag around $(2, 1)$ and $(3, 1)$, which is consistent to the groundtruth and the model in Eq.(11). In addition to the position of water bag, we also estimate the displacement of the water bag based on the reflection phase matrix. In Figure 7(b),

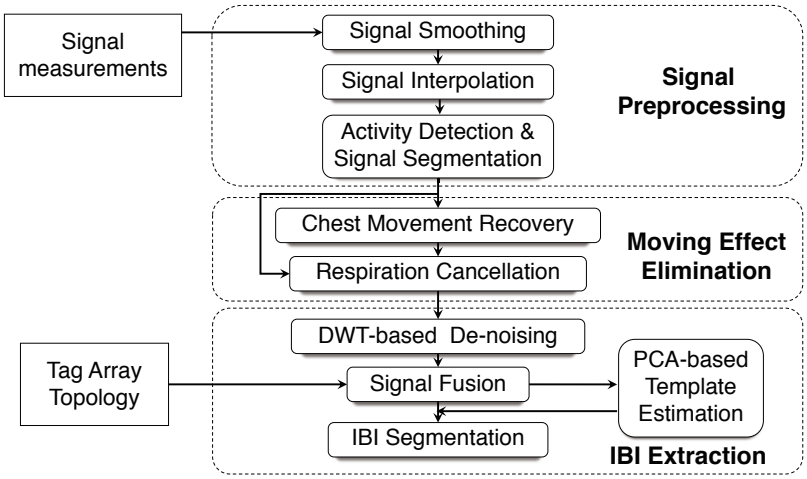

Fig. 8. System Architecture.

the maximum reflection phase range is 8.4 radian of the tag at (2, 1), which represents the displacement of about 22*cm*. The estimated displacement is very close to the groundtruth, which is 20*cm* according to the deployment. Therefore, the experiment results validate the effectiveness of our reflection model of the tag array.

4 RF-ECG SYSTEM DESIGN

4.1 System Overview

The system architecture of RF-ECG is shown in Figure 8. To perform the HRV assessment, a set of COTS RFID tags are attached in the chest area on the clothes of the human subject, which forms a tag array for comprehensive sensing. A COTS RFID reader is deployed to continuously interrogate these tags by issuing a *continuous wave*, and collect their *backscattered RF-signals* within the effective scanning range (1 ∼ 3m). According to the received RF-signals from the tag array, we leverage three main components in RF-ECG to extract the HRV information, i.e., *Signal Preprocessing*, *Moving Effect Elimination* and *IBI Extraction*. *Signal Preprocessing* first filters the received RF-signals from the tag array with smoothing and interpolation, and then detects the activities of human body to segment the signals for the following HRV estimation. *Moving Effect Elimination* removes the respiration influence by estimating the contour of chest movement and cancels the phase variation caused by the *moving effect*. *IBI Extraction* further extracts the Inter-Beat Interval (IBI) from the reflection signal captured by the tag array. Specifically, we first use Discrete Wavelet Transform (DWT) to further reduce the ambient noises by concentrating on the heartbeat frequency band. We then fuse the RF-signals from the 2-dimensional tag array into a signal sequence to generate a clear periodic pattern. We further coarsely segment the fused signal and use the Principal Component Analysis (PCA) to obtain a template to depict the principle features of a heartbeat period. Finally, we estimate a fine-grained IBI segmentation by maximizing the similarity between the signal segments and the template based on dynamic programming. The extracted IBI can be further used for HRV assessment.

4.2 Signal Preprocessing

According to the empirical study in Section 3.2, for the RF-signals from the tag array, the *heartbeat signal* is almost buried by the *respiration signal* and the ambient noise. Hence, after we obtain the RF-signals from the tag array, it is essential to smooth the collected signal for further extraction of the *heartbeat signal*. According to [40], the phase noises of RF-signals follow the Gaussian distribution. Therefore, we use Kalman filter [20] to process

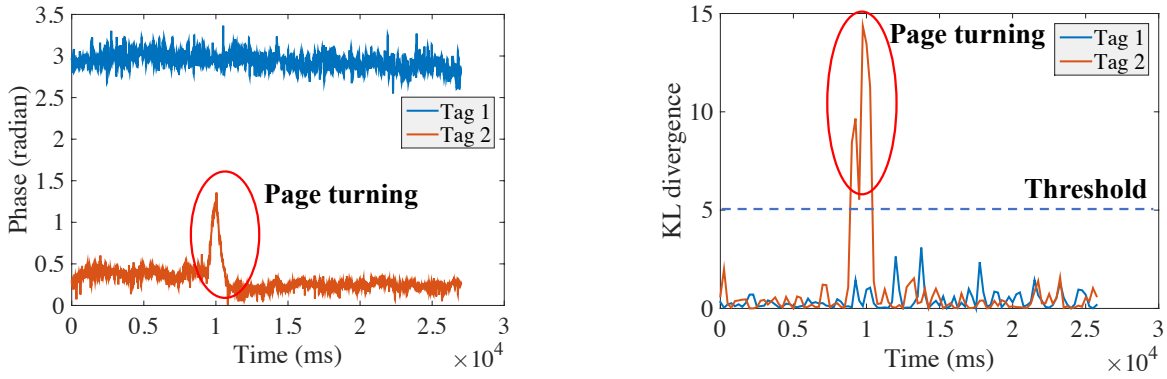

(a) Raw phase sequences of two tags

(b) KL divergence sequences of two tags

Fig. 9. Calculating KL divergence from the phase sequence.

the raw phase sequence of the RF-signals, which reduces the ambient noises but keeps the signals caused by the respiration and heartbeat.

Moreover, in COTS RFID system, the EPC Gen2 standard [32] adopts a framed slotted Aloha protocol to interrogate the tags in a random manner, which makes the uniform sampling over the tags impossible. To tackle this issue, assuming that the phase sequences change continuously, we use a cube spline interpolation method [13] to resample the phase sequence with uniform sampling rate. In particular, we resample the phase sequence with the sampling interval of 4 ms.

Next, we demonstrate to segment the signal sequence for IBI estimation according to the activeness of the user. Since RF-ECG is designed to estimate the IBI in a relative stationary environment, we need to firstly remove the signal sequence with apparent fluctuations due to the larger activities, and then focus on the other stable signal for the IBI estimation. Toward this end, we design an adaptive scheme to calculate the activeness of the user based on the KL divergence [15]. For the signal sequence, we use a sliding window to divide the sequence, and calculate the discrete probability distribution function (PDF) of the signal within the window. Then given the PDF of two consecutive windows P and Q, the KL divergence is defined as:

$$D_{KL} = \sum_i P(i) \cdot \ln \frac{P(i)}{Q(i)}, \tag{14}$$

where $P(i)$ and $Q(i)$ is the probability value of index i.

The KL divergence measures the information loss when the distribution Q is used to approximate the distribution P. Thus, a large value of the KL divergence indicates a large activity of the user, which leads to large difference between distribution P and Q. Figure 9 presents two KL divergence sequences calculated from two phase sequences: the signal of tag 1 contains an activity of page turning and the signal of tag 2 contains only small activities such as breathing. Based on the KL divergence, we can clearly detect the activity of page turning, which have larger KL divergence value compared with the empirical threshold.

For the detected activities based on the KL divergence, we can classify them based on the activity duration into two kinds, *i.e.*, long activity ($> 2s$) and short activity ($\leq 2s$). For the long activity, we just skip the sequence, because these activities are related to the movement of the whole human body, and thus the signal sequence is too noisy for the fine-grained IBI estimation. In regard to the short activity, it is usually caused by the small actions, *e.g.*, page turning, scratching or shrugging. Since the human body almost stays at the same position, we can remove the sudden phase change due to the small actions and still leverage the scheme in Section 4.5 for the

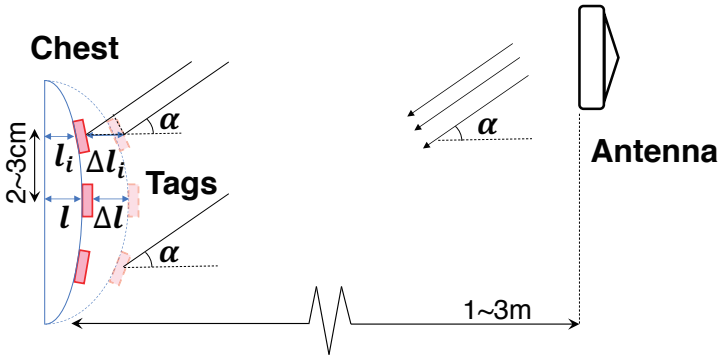

Fig. 10. Modeling the moving effect.

IBI estimation. As the small action has low frequency compared with the heart rate, we use a Butterworth filter to remove the sudden phase change.

4.3 Moving Effect Elimination

After signal preprocessing, we obtain a sequence of RF-signals mixed with the *respiration signal* and the *heartbeat signal*. Then, it is essential to extract the *heartbeat signal* from the reflection effect by removing *respiration signal* from the moving effect. Here, the *moving effect* means that the RF-signal changes along with the chest movement due to respiration, whereas the *reflection effect* means that the RF-signal changes due to the reflection from the heartbeat movement. According to the empirical study in Section 3.2, the respiration brings much larger influence to the received RF-signals than the heartbeat. Therefore, to estimate the *respiration signal* from the raw phase changes of the RF-signal, we can roughly neglect the phase changes due to the *reflection effect* and regard the phase changes are mainly caused by the *moving effect*.

In this paper, we propose a tag array-based mechanism to estimate and eliminate the *respiration signal*. Specifically, we first estimate the contour of chest movement through a physical model between the tag array and chest. Then, we calculate the phase change of each tag corresponding to the chest movement for signal elimination. As shown in Figure 10, the respiration process can be modeled as the back-forth displacements of the chest. We set the chest contour at time t_0 as the reference contour. During the process of chest displacement, for an arbitrary time t, we use $\Delta l(t)$ to denote the largest displacement of the chest contour, which is usually corresponding to the displacement of the chest's midpoint; we also use $\Delta l_i(t)$ to denote the displacement of each tag T_i from the tag array. Assume the displacement of the chest contour follows a linear relationship, then, the displacement $\Delta l_i(t)$ of each tag T_i has a fixed scale factor $\zeta_i = \frac{\Delta l_i(t)}{\Delta l(t)}$ with respect to the displacement $\Delta l(t)$ for any time t. The value of ζ_i depends on the relative position of the tag T_i on the chest.

Suppose the incident angle of the signals from the antenna, i.e., the angle between the transmission direction of the antenna and the horizontal plane, is α. Since the antenna is deployed fairly far away from the human subject (e.g., $1 \sim 3m$), whereas the distance between each tag is very close (e.g., $2 \sim 3cm$), the incident angle α of the antenna can be regarded as uniform for different tags. Then, the phase variation of tag T_i can be derived from Δl_i as follows:

$$\Delta\theta_i = \frac{2\pi\Delta l_i \cos\alpha}{\lambda/2} \mod 2\pi, \tag{15}$$

where λ is the wave length. Since the chest displacement is usually smaller than half of the wavelength (i.e., $16.2cm$), we neglect the modulo operation in following derivation.

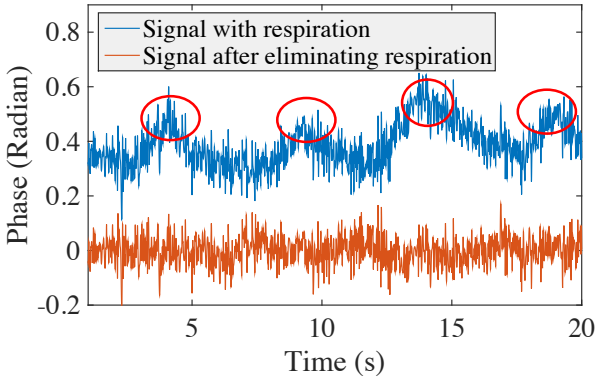

Fig. 11. Eliminating the moving effect from the mixed RF-signals.

Hence, suppose there are n tags on the tag array, if we can obtain the scale factor ζ_i for different tags, the largest displacement of chest contour Δl can be estimated as follows:

$$\widehat{\Delta l} = \frac{1}{n}\sum_{i}^{n}\frac{\Delta l_i}{\zeta_i} = \frac{\lambda}{4n\pi\cos\alpha}\sum_{i}^{n}\frac{\Delta\theta_i}{\zeta_i}. \tag{16}$$

Once we have the displacement $\widehat{\Delta l}$, we can derive the phase change of each tag T_i during the respiration process as follows:

$$\widehat{\Delta\theta_i} = \frac{4\pi\widehat{\Delta l_i}\cos\alpha}{\lambda} = \frac{4\pi\widehat{\Delta l}\zeta_i\cos\alpha}{\lambda} = \frac{\zeta_i}{n}\sum_{i}^{n}\frac{\Delta\theta_i}{\zeta_i}. \tag{17}$$

Then, we can subtract the estimated phase sequence $\widehat{\Delta\theta_i}$ from the filtered phase sequence, so as to remove the interference from the *respiration signal*.

Based on the above analysis, it is critical to estimate the parameter ζ_i for different tags, we thus depict the solution as follows: Suppose for each tag T_i, the interpolated phase sequence from a specified time window W is $\Theta_i = \{\theta_i(t)\}$. For any time $t \in W$, we can add the phase of different tags together as $\theta_s(t) = \sum_{i=1}^{n}\theta_i(t)$, and obtain the phase sequence $\Theta_s = \{\theta_s(t)\}$. In this way, we are able to obtain the principal phase variation trend of all tags. According to the time points of each adjacent peak and valley in Θ_s, say t_j and t_{j+1}, which is corresponding to the largest displacement of the chest contour $\Delta l(t)$, we can calculate the corresponding phase change in Θ_i for any tag T_i, and obtain the averaged phase change from m samples as follows:

$$\beta_i = \frac{1}{m}\sum_{j=1}^{m}|\theta_i(t_{j+1}) - \theta_i(t_j)|. \tag{18}$$

As the displacement $\Delta l(t)$ is uniform for all tags, hence the value of β_i is proportional to the value of ζ_i, i.e., $\zeta_i = \beta_i \cdot C$, C is a constant. According to Eq.(17), we can replace ζ_i with β_i and compute the value of $\widehat{\Delta\theta_i}$.

Figure 11 shows an example of eliminating the moving effect of respiration from the mixed RF-signals. In the signal with respiration, we use the red circle to mark the signal change due to the moving effect, which periodically arises based on the respiration pattern. Note that after the elimination, the periodic peaks and valleys caused by the respiration are almost removed. We can observe some periodicity for the remaining signals, which is corresponding to the heartbeat.

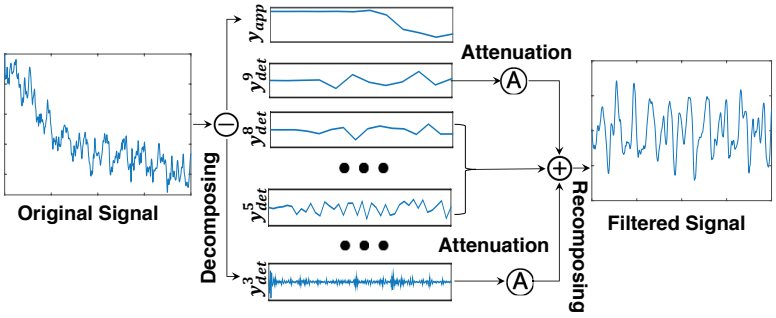

Fig. 12. Illustration of DWT denoising flow.

4.4 DWT-based Denoising

After eliminating the respiration signal caused by the moving effect, there still exist some noises in the remaining signals, as the approximated respiration signal derived from the moving effect cannot completely be consistent with the actual respiration signal. Hence, we use the Discrete Wavelet Transform (DWT)-based denoising method to further remove the noises from the remaining signals. Compared with other filtering techniques, the Discrete Wavelet Transform can analyze the signal in both time and frequency domain without making any assumption about the nature of the signal. It decomposes the signals into the approximation coefficients and the detailed coefficients. The approximation coefficients denote the low frequency signals, which correspond to the residual components of the respiration signals. The detailed coefficients denote the signal details of the heartbeat as well as the high frequency noises. As the heartbeat usually falls in the frequency range of $1 \sim 2Hz$, we are able to further remove the residual noises by filtering out both the approximation coefficients and the detailed coefficients in higher frequency band.

In particular, the DWT method includes three steps. 1) *Decomposition*: We first run the DWT-based signal decomposition recursively by 9 levels with Symlet wavelet filter [33]. The DWT generates the approximation coefficients y_{app} and a sequence of detailed coefficients $y^1_{det}, y^2_{det}, \cdots, y^9_{det}$, where y^1_{det} has higher frequency than y^9_{det}. 2) *Filtering*: We apply the filtering method to extract the components corresponding to the heartbeat frequency band. In particular, we remove the approximation coefficients y_{app} which is related to the large displacement from chest movement. Meanwhile, we keep the detailed coefficients $y^5_{det}, \cdots, y^8_{det}$ unchanged, which correspond to the frequency about the heart beat (ranging from $0.7Hz$ to $5.6Hz$). In regard to the other components, since they are mainly related to the noisy signal, we reduce them to 20% according to our empirical study, which can remove most noise and keep the sufficient details about heart beat. 3) *Reconstruction*: By combining all the remaining coefficients (i.e., the detailed coefficients after filtering), we reconstruct the final phase trends with the inverse DWT as follows: $\{\widehat{\theta}'_i(1), \cdots, \widehat{\theta}'_i(t)\}$. The reconstructed measurements enable us to remove the noise components while keeping the heartbeat related phase signal. In Figure 12, we show an example to illustrate the DWT denoising flow. Note that after DWT, the original decreasing trend of the signals is removed, while the detailed heartbeat influence remains. Therefore, DWT facilitates accurate inter-beat interval estimation, when the respiration signal is not fully removed.

4.5 Signal Fusion from RFID Tag Array

After denoising the signals based on DWT, we can observe fairly clear periodic pattern caused by the heartbeat from these signals. According to the model in Section 3.3, the current signals S_r still contain two components, i.e., $S_{r,0}$, which is the mixture of LOS signal and reflection signal from the static background environment, and $S_{r,1}$, which is the reflection signal from the heartbeat movement. Since it is difficult to measure the signal $S_{r,0}$ like Section 3.3 by simply removing the heartbeat, we can select a sufficiently large time interval, and use the averaged

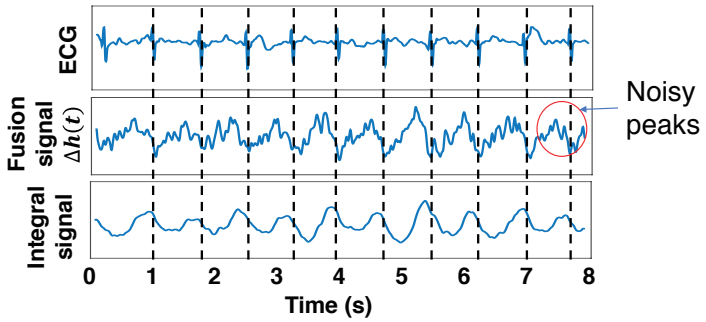

Fig. 13. Signal fusion result vs the ECG ground truth.

signals of S_r to estimate $S_{r,0}$. As the reflection signal $S_{r,1}$ from the heartbeat varies periodically, during the process of averaging, the variable component $S_{r,1}$ mutually offsets each other, and finally the constant component $S_{r,0}$ is estimated.

So far, the reflection signal $S_{r,1}$ from the heartbeat could be obtained. However, the signals from any single tag usually cannot precisely depict the state change of the heartbeat, due to the following reasons. 1) *Tag misreading*: Due to the issues such as the energy absorption, some tags may fail to capture the reflection signals of heartbeats frequently due to tag misreading. 2) *Different sensitivities*: As the tags are deployed in different positions of the tag array, their sensitivities to the reflection effect are different according to our empirical study. To address the above issues, we further fuse multiple signals of different tags from the tag array to estimate the state change of heartbeat. Specifically, we first estimate the position of the heart according to the reflection model in Section 3.3, and then use the method of Minimal Mean Square Error (MMSE) to estimate the heartbeat displacement by fusing the signals from the tag array.

We first estimate the heart position according to the reflection signals from the tag array. For a selected time interval W, we can continuously capture the phase change $\Delta\theta_i^r(t)$ of each tag T_i. Then, we can compute the average phase change as $\overline{\Delta\theta_i^r}$ within the time interval W. According to Eq (11), the average phase change $\overline{\Delta\theta_i^r}$ is corresponding to an average heart displacement $\overline{\Delta h}$, i.e.,

$$\overline{\Delta\theta_i^r}(\overline{\Delta h}) \approx \frac{2\pi\overline{\Delta h}(\cos\phi_i + \cos\phi_A)}{\lambda} \mod 2\pi, \tag{19}$$

where the modulo operation can be neglected due to the small displacement of the heartbeat. Therefore, after measuring and averaging the phase changes of reflection signal, we can obtain $\overline{\Delta\theta_i^{r*}}$. In comparison to the theoretical value $\overline{\Delta\theta_i^r}(\overline{\Delta h})$, we use the MMSE to estimate the heart position (x_B, y_B, z_B) as follows:

$$\arg\min_{x_B, y_B, z_B, \overline{\Delta h}} \sum_{i=1}^{n} (\overline{\Delta\theta_i^r}(x_B, y_B, z_B, \overline{\Delta h}) - \overline{\Delta\theta_i^{r*}})^2. \tag{20}$$

As the relative position of the antenna $\mathcal{A}$ cannot be obtained in advance, the value of $\cos\phi_A$ is unknown. Nevertheless, since it is a constant value for all tags, we can cancel $\cos\phi_{\mathcal{A}}$ from the object function by subtracting the phase of a specified tag (e.g., tag T_1) :

$$\arg\min_{x_B, y_B, z_B, \overline{\Delta h}} \sum_{i=1}^{n} ((\overline{\Delta\theta_i^r} - \overline{\Delta\theta_1^r}) - (\overline{\Delta\theta_i^{r*}} - \overline{\Delta\theta_1^{r*}}))^2. \tag{21}$$

A straightforward solution is to enumerate all the possible combinations of x_B, y_B, z_B, and $\overline{\Delta h}$, which is rather time consuming. In fact, according to some priori knowledges, we are able to greatly reduce the infeasible

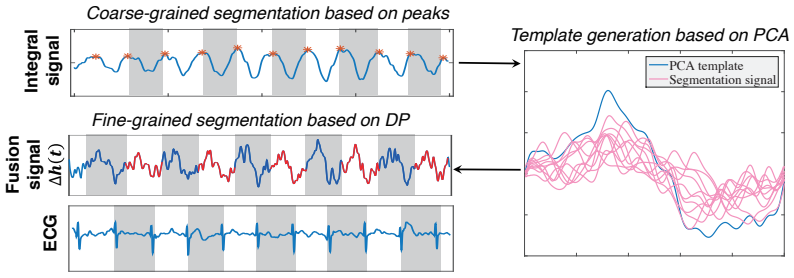

Fig. 14. An example of IBI Segmentation

solutions to reduce the compute complexity. For example, the empirical study in Section 3.3.3 shows that the tag close to the heartbeat usually have relatively large phase changes. Hence, x_B and y_B can be reduced to a small range based on the actual phase distribution. Similarly, z_B and $\overline{\Delta h}$ can be reduced to a small range based on the physical structures of human body.

After figuring out the position of heartbeat, we further estimate the heart displacement $\Delta h(t)$ at time t. Specifically, according to Eq (11), as the modulo operation can be neglected, the theoretical phase change of each tag T_i at time t is

$$\Delta\theta_i^r(\Delta h(t)) = \frac{2\pi\Delta h(t)(\cos\phi_i + \cos\phi_A)}{\lambda}. \tag{22}$$

Hence, after measuring the phase changes $\Delta\theta_i^{r*}(t)$ for each tag T_i at time t, let $\gamma_i(t) = (\Delta\theta_i^r(t) - \Delta\theta_1^r(t))$, and $\gamma_i^*(t) = (\Delta\theta_i^{r*}(t) - \Delta\theta_1^{r*}(t))$, then we utilize MMSE to estimate $\Delta h(t)$ as follows:

$$\Delta h(t) = \arg\min_{\Delta h(t)} \sum_{i=1}^{n} (\gamma_i(t) - \gamma_i^*(t))^2. \tag{23}$$

Figure 13 plots an example signal wave of the heartbeat movement $\Delta h(t)$. For the better comparison, we respectively plot the ground truth of ECG signal and the *fusion signals* of $\Delta h(t)$. It is found that the periodic pattern can be clearly observed from the *fusion signals*. However, we also observe some noisy peaks among the waveforms, which is due to the weak reflection of the heartbeats.. Therefore, we further compute the integral of the fusion signals to obtain the *integral signals* which are more smooth. Note that the mean value of the *fusion signals* is moved to 0 after eliminating the moving effect, so the integral process does not incur obvious error accumulations. After the integral smoothing, most noisy peaks are removed in the *integral signals*, such as to clearly obtain the profiles of the phase sequence.

4.6 Inter-Beat Interval Segmentation

At last, we estimate the Inter-Beat Interval (IBI) based on the fusion signal. Similar to [42], we leverage a dynamic programming-based approach to estimate each IBI. The intuition is that, even if the heartbeat may have different inter-beat intervals, the overall shape of each heartbeat should be quite similar. Hence, our solution is to find the segmentation that maximizes the correlations between each segment. Different from [42], which takes a long time to iteratively search for the optimal segmentation and template, we design a PCA-based algorithm to learn the template for further segmentation. In particular, we first coarsely segment the integral sequence by detecting the peaks, since we can clearly observe the periodic wave from the integral signal in Figure 13. Then, we re-sample each segment to the same length for template study. Finally, we can learn the template from all the segments with the same length, which is further used for fine-grained segmentation.

Figure 14 shows an example of IBI Segmentation, we first segment the *integral signals* by detecting the peaks as a coarse-grained segmentation. Here, small peaks are removed as false segmentations. We further apply the

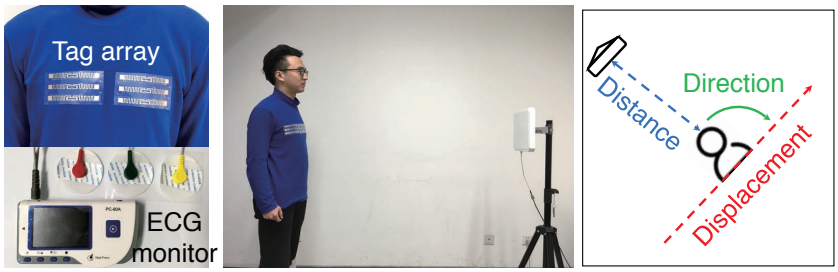

Fig. 15. Experiment setup.

coarse-grained segmentation on the fusion signals. Then we re-sample each segment to the same length and use PCA to learn the principle shape from all these segments to obtain a template $\mathbf{T}_f$. Since each segment indicates one heartbeat, the principle shape of these segments can well depict the feature of one heartbeat in a statistical manner. Based on this template, we further leverage Dynamic programming for fine-grained segmentation. Suppose $\mathbf{S}_f = \{\mathbf{s}_f(1), \mathbf{s}_f(2), \cdots\}$ is the segmentation on the *fusion signal*, our solution aims to maximize the correlations between each segment and the template as follows:

$$\mathbf{S}_f = \arg\max_{\mathbf{S}_f} \sum_{\mathbf{s}\in\mathbf{S}_f} corr(\omega(\mathbf{s}, |\mathbf{T}_f|), \mathbf{T}_f), \tag{24}$$

where $\omega(\mathbf{s}, |\mathbf{T}_f|)$ resamples $\mathbf{s}$ to the same length of the template $\mathbf{T}_f$ and $corr()$ calculates the correlations between the segment and the template. As shown in Figure 14, it is found that the segmentation result is very close to the ground truth of ECG with the error in several milliseconds. The fusion segments lag behind the ECG ground truth because the heartbeat movement usually lags behind the electronic signal.

In regard to the complexity of the algorithm, since we leverage dynamic programming to solve the problem, the time complexity is $O(n)$, where n represents the signal length. In comparison, the state-of-the-art algorithm [42] alternatively update the segmentation and template, which leads to $O(kn)$ time complexity. Here, k is the number of iteration, which is on average 8 during the execution. Therefore, our method can save a lot of time from the iteration.

5 PERFORMANCE EVALUATION

5.1 Experimental Setup & Methodology

Implementation. We implemented RF-ECG based on COTS RFID devices: ImpinJ Speedway modeled *R*420 RFID reader, Laird *S*9028*PCL* directional antenna, Impinj ER-62 and Impinj E41-B tags. As shown in Figure 15, we deployed a tag array on the chest area in the clothes of the human subject for heartbeat sensing, whose topology was used as input of our algorithm. During the experiments, the reader continuously interrogated the tags in front of the user to collects RF-signals for IBI estimation.

Setup. In our experiments, we let 15 volunteers (12 males and 3 females, aging from 21 to 55) measure the heartbeat through RF-ECG in front of the antenna with different setups and user conditions. During the experiments, the antenna was placed with the same hight of the chest, when he/she sits/stands in front of the antenna. As shown in Figure 15, we had four main parameters in our experiments setup: 1) *distance*: we changed the distance between antenna and user from $1m$ to $2.5m$; 2) *direction*: we changed the facing direction of user from $-30°$ to $30°$; 3) *displacement*: we changed the displacement of the user related to the beam of the antenna from $-60cm$ to $60cm$; 4) *tag array size*: we changed the tag array size from 4 tags to 9 tags. To compare with the traditional device-free methods, we also changed the number of users monitored by RF-ECG, and used RFID tags to distinguish them for the IBI estimation of each user. Meanwhile, six different conditions of the volunteers were considered: *hold*

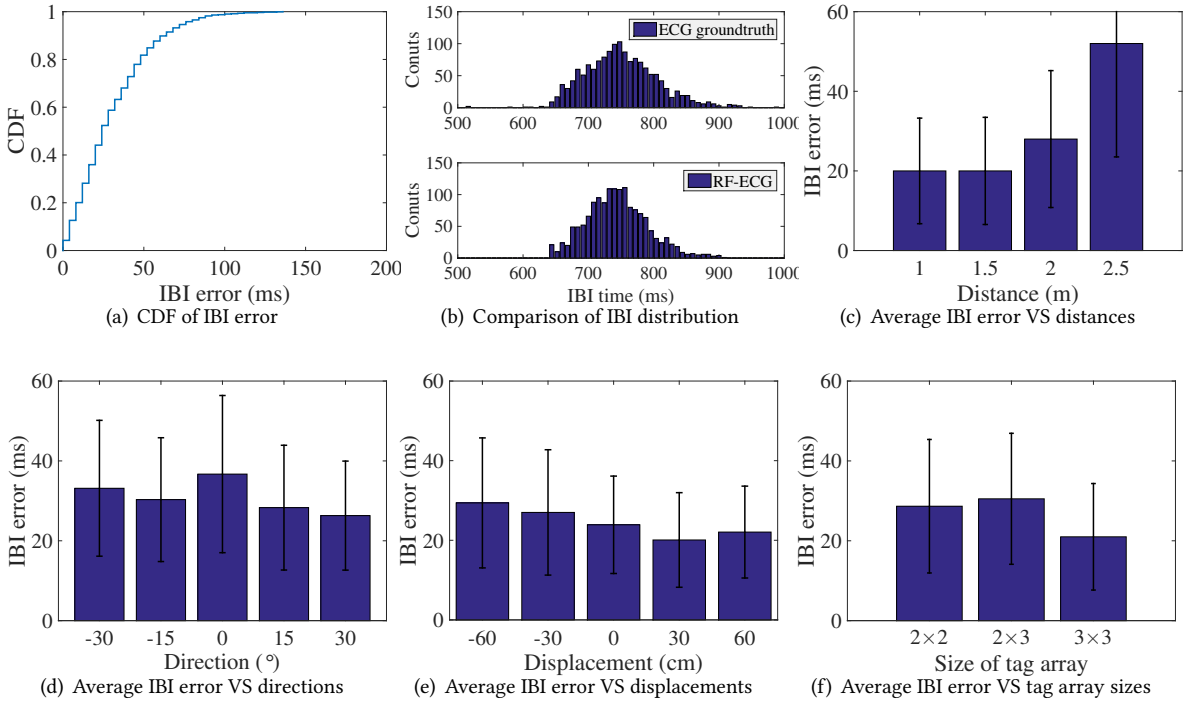

(a) CDF of IBI error
(b) Comparison of IBI distribution
(c) Average IBI error VS distances
(d) Average IBI error VS directions
(e) Average IBI error VS displacements
(f) Average IBI error VS tag array sizes

Fig. 16. Evaluate the accuracy of IBI with different parameters.

breath, *sit*, *stand*, *sleep*, *recline* and *after exercise* to evaluate the robustness of our system, which indicate the possible user conditions in real monitoring environment. Besides, five small activities were also considered: *talking*, *snoring*, *typing*, *drinking* and *page turning* to evaluate the performance of RF-ECG, which indicates the possible daily activities. In each case, we collected the measurement from RF-ECG for 30 seconds and we repeated the experiment with the given set of parameters for 10 times, which contains about 12,000 heartbeats for each parameter set. The default setup was the volunteer attached with 6 tags sits $1.5m$ away from the antenna with 0° direction and $0cm$ displacement.

Metrics. We use the *IBI error*, which calculates the time difference between the measured IBI time and the groundtruth of ECG to evaluate RF-ECG. We collect the groundtruth from the Heal Force PC-80A ECG Monitor as shown in Figure 15.

5.2 IBI Estimation with Different Setups

Experimental results show that RF-ECG achieves a median error of 24ms compared with the ECG groundtruth. We first present the CDF figure of the IBI error in Figure 16(a). The median error based on our experiments is $24ms$, which is only 3% error with respect to the average IBI duration. The jump of CDF is caused by the interpolation resolution in our system. According to the results, more than 80% of our measurements have an IBI error within $50ms$, which indicates an IBI accuracy of about 93%. Therefore, RF-ECG can achieve good accuracy in estimating the IBI with different setups. We further compare the distribution of the measured IBIs using RF-ECG and the ECG groundtruth as shown in Figure 16(b). We could see the distributions are quite similar to each other, which indicates the accuracy of our estimation. Both the distribution peaks are around $740ms$, which is the common IBI value in daily life.

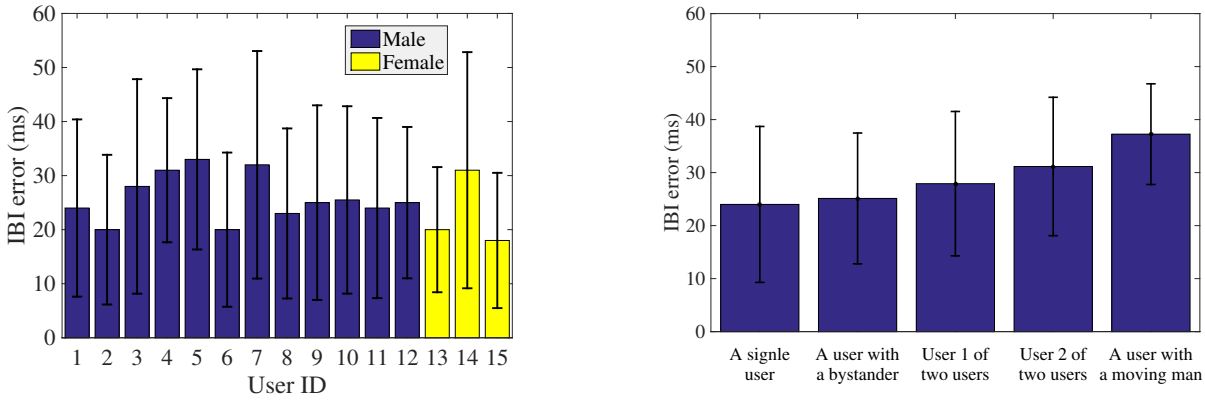

(a) IBI accuracy across different users

(b) IBI error when measuring multiple users simultaneously

Fig. 17. IBI accuracy across different users and multiple users.

Experimental results show that RF-ECG achieves an average IBI error of 30.4*ms for all experiments, while the IBI error increases as the distance increases.* We next change four main parameters in the experiment setup, i.e., distance, direction, displacement and the size of tag array to evaluate the robustness of RF-ECG. Figure 16(c)~16(f) show the corresponding average IBI errors when we vary the four parameters. As the volunteer moves away from the antenna, the average IBI error increases gradually in Figure 16(c), because the RF-signal fades quickly with the increment of transmitting distance. However, we can still achieve a small average IBI error of 28*ms* at 2*m*, which provides a large coverage region for heartbeat monitoring. In addition, the IBI errors do not vary obviously along with the directions in Figure 16(d). The average IBI errors are all below 30*ms*, which indicates the robustness of RF-ECG. Moreover, we can observe the error slightly decreases for directions of 15° and 30°. The reason is when the volunteer rotates to the right side, the heart becomes closer to the antenna, which increases the reflection influence of the heart. Figure 16(e) also shows similar trends in displacement. As the volunteer moves to the right sides with the increment of the displacement, the IBI errors slightly reduce, because the influence of the right part of the body to the RF-signal becomes smaller. In regard to the size of tag array, we note that the IBI error also decreases when we use more tags as shown in Figure 16(f). We also find that the 2×2 tag array has slightly lower IBI errors compared with the 2×3 tag array. It is probability because the distance between adjacent tags in the 2×3 tag array is relative smaller, and the small distance affects the signal of nearby tags. In this case, the distance between adjacent tags have larger influence compared with the increment of tag number. Overall, the results indicate that RF-ECG can benefit from the increased numbers of tags for comprehensive heartbeat monitoring based on our model.

5.3 IBI Estimation with Different Users and Different Number of Users

Experimental results show that RF-ECG achieves good IBI accuracy with different users, ages and genders. Next we examine the robustness of RF-ECG by evaluating the IBI accuracy with different users. We ask 15 volunteers (12 males and 3 females) to measure the heartbeat using RF-ECG with the default setup. Figure 17(a) presents the estimation IBI results of each user. We find the IBI errors are similar across different volunteers. Specifically, the average IBI errors of all the volunteers are within 35*ms*, while four of them are within 20*ms*. We note that two of the three girls have average IBI error within 20*ms*. In regard to the old man (*e.g.*, User 12), we can also achieve an IBI error of 25*ms*, which is comparable with other users. In regard to the difference of IBI errors across different users, we think it may be caused by the different body shapes of the volunteers, which may distort the wireless

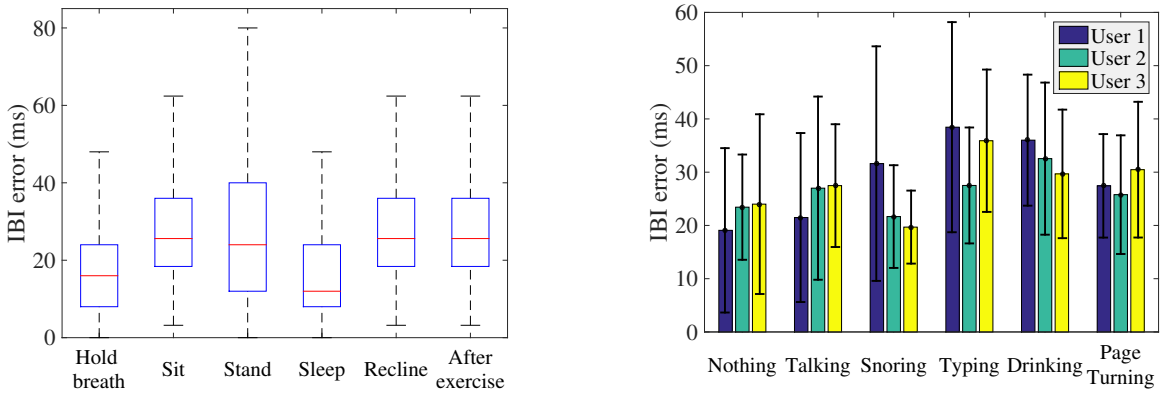

(a) IBI accuracy of different static conditions

(b) IBI error of different activies

Fig. 18. IBI accuracy across different user conditions.

signal differently and lead to different IBI errors. Therefore, it is convincing that RF-ECG is applicable to monitor different users regardless of the genders or ages.

Moreover, we also examine the performance of RF-ECG, when multiple people are in the monitoring range of RF-ECG at the same time. Particularly, we consider three typical scenarios: 1) one target user for IBI monitoring with one bystander, where the bystander just stands around the target user without attaching any RFID tags; 2) two target users for IBI monitoring simultaneously; and 3) one target user for IBI monitoring with a moving man, where the man keeps walking randomly around the target user to change the ambient environment. We compare the IBI errors of the three scenarios with the default scenario, where only one target user is in the monitoring range of RF-ECG. Figure 17(b) presents the estimation results for the four scenarios. We find that we can achieve similar estimation accuracy, even though one bystander is around the target user. It indicates RF-ECG can efficiently distinguish the target user from other people for IBI estimation. Moreover, when we monitor the IBI of two target users simultaneously, the IBI errors increase to about 30*ms*. The reason is that the RFID system utilizes the slotted ALOHA protocol for the tag identification, so the increment of target user number will reduce the sampling rate for each tag, affecting the final accuracy of IBI estimation. However, the IBI errors of about 30*ms* can still provide sufficient information for the treatment of heart diseases. Besides, when a man is walking around the target user, the estimated error increases to 39*ms*, which indicates the change of ambient environment will affect the measuring result to some extend. Therefore, the stability of ambient environment will improve the estimation accuracy during the monitoring. On the other, in the last case RF-ECG can still achieve 39*ms* estimation error, indicating the IBI estimation can be still used as the clue for the treatment of heart diseases.

5.4 IBI Estimation with Different Conditions and Activities

RF-ECG can achieve an average IBI error of 25.6*ms when the user is under different conditions.* We further evaluate the performance of RF-ECG, when the users measure the heartbeats in different conditions. In particular, six conditions, *i.e.*, *hold breath*, *sit*, *stand*, *sleep*, *recline* and *after exercise*, are considered in our experiments. Normally, the volunteer sits on the chair to measure the heartbeat. For the stand case, the volunteer stands still in front of the antenna; for the sleep case, the volunteer lies on the bed under the antenna; for the recline case, the volunteer reclines on the safe in front of the antenna. As shown in Figure 18(a), we use boxplot to show the distributions of IBI errors of each condition. We find the average IBI errors are all below 30*ms*, which represents the high accuracy of RF-ECG. When the volunteer holds the breath, we achieve the small IBI error of 16*ms*, because the chest movement is minimized in this condition. For the sleep case, we also achieve very small IBI error of 14*ms*,

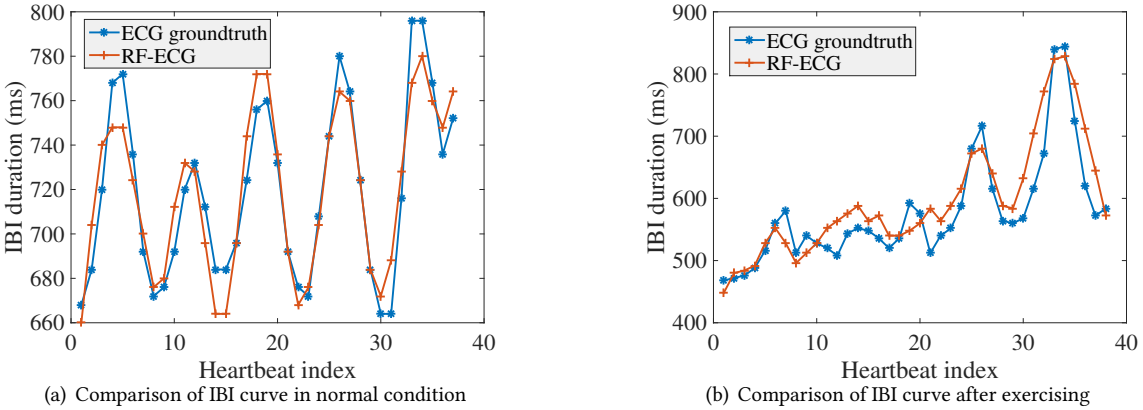

(a) Comparison of IBI curve in normal condition

(b) Comparison of IBI curve after exercising

Fig. 19. IBI curve comparison with the ECG groundtruth.

because the human body is usually still during sleeping, leading to small noise. As the volunteer stands up, the variance of IBI error increases. This is because the human body can unavoidably waggle when standing up, which introduces some signal noise. When the volunteer reclines on the sofa, the IBI error is a little larger than other cases, because this posture may distort the relative positions of tag array, and finally affect the IBI estimation. When the user measures heartbeat after exercising, we can still achieve a small IBI error. The reason is that after exercising, the heart will beats quickly and intensely, which leads to clear reflection for estimation. But since the heart rate changes quickly after exercise, the variance is also larger than other conditions.

In addition to these monitoring conditions, we also consider some typical small activities in daily life. In particular, *talking*, *snoring*, *typing*, *drinking* and *page turning* are considered in our experiments. Three young men perform these activities during the IBI monitoring. Figure 18(b) compares the corresponding IBI errors of these activities with the default scenario, when the volunteers sit still with no activities. We find that the talking and snoring activities have similar IBI error with the nothing case, because talking and snoring only incurs small chest movement like breathing. As for the other three cases, since they all incur small body movement during the activities, we need to cancel the phase distortion due to the activities. These cancellation can not perfectly remove the phase distortion, leading to residual phase noise and large IBI errors. Overall, the IBI errors are all below 40*ms*, which indicates RF-ECG can efficiently monitor the IBI during the small activities.

5.5 Comparison of IBI Curve

Experimental results show that RF-ECG is able to capture the fine-grained feature of HRV from the estimated IBI. We compare the detailed IBI curve with the ECG groundtruth of two different conditions as shown in Figure 19. The IBI curve depicts the variation trend of estimated IBIs in time domain. Based on the comparison, we find the IBI curve of RF-ECG is close to the ECG ground truth and the peaks are matched perfectly. When the volunteer measures the heartbeat in a default sitting condition, we find a period pattern of the IBI curve in Figure 19(a). In actual, such periodic pattern of IBI sequence is called *Respiration Sinus Arrhythmia* (RSA), which has been used as an index of cardiac vagal function [29]. The periodic ups and downs of the IBI values is along with the chest movement due to respiration. Therefore, the results indicates that the IBI estimation from RF-ECG is able to conduct fine-grained HRV analysis. Figure 19(b) shows the slow down of heartbeat after exercising. The matching curve indicates RF-ECG can accurately detect the variation of IBI due to exercises. Moreover, at the end of the curve, we also detect the RSA phenomenon, which shows the efficiency of RF-ECG. The results indicates that RF-ECG is able to efficiently detect the variation of IBI due to different reasons, e.g., exercise or RSA.

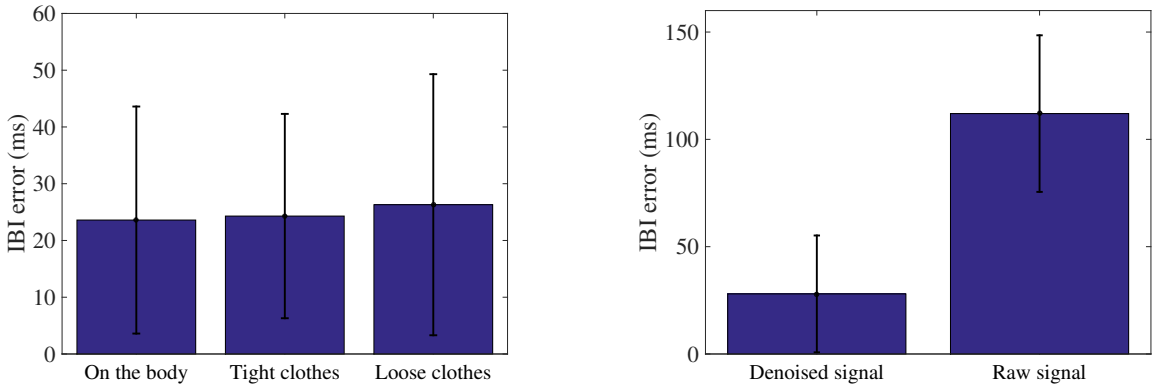

(a) IBI error across different kinds of clothes

(b) Performance evaluation of the denoising method

Fig. 20. IBI accuracy across different kinds of clothes and denoising methods.

5.6 IBI Estimation with Different Kinds of Clothes

RF-ECG can achieve less than 27ms average IBI errors for different kinds of clothes. Next, we evaluate the impact of the clothes type on the IBI estimation. Three types of clothes are considered in our experiments: tight clothes, loose clothes and directly on the body [1]. Figure 20(a) presents the IBI results of the three types. We find that tighter clothes can achieve smaller IBI errors, because the tags are closer to the heart with the tighter clothes and thus can receive clearer heart signal. However, the impact of the tightness of clothes is relatively small, as we can still achieve high IBI accuracy (*i.e.*, 26.3*ms* error) based on the loose clothes. Therefore, RF-ECG is suitable to handle different tightness of the clothes for the IBI estimation.

5.7 IBI Estimation with/without Denoising Method

The denoising method proposed in RF-ECG can efficiently remove the noisy signal for accurate IBI estimation. Finally, we examine the effectiveness of the denoising method in RF-ECG by comparing the IBI errors estimated based on the denoised signal and the raw signal without denoising method. Figure 20(b) presents the comparison of the corresponding IBI errors. It is clear that the denoised signal outperforms the raw signal, which is about 4 times better on the IBI error. Even though the raw signal contains the signal change due to the heart beat, it also contains different kinds of noisy signals (*e.g.*, the chest movement and body movement). Therefore, the denoising method in RF-ECG is essential and efficient for the accurate IBI estimation.

6 DISCUSSION

Limitations. Even though RF-ECG can achieve accurate IBI estimation compared with the traditional ECG-based approaches, there are still some limitations when performing RF-ECG in the real environments. 1) Due to the limitation on the communication range of RFID tags, the users are supposed to be close to the antenna (within 3*m*) for accurate and efficient HRV measurement. Based on the understanding, indoor HRV monitoring is more suitable, where one RFID antenna can cover the primary activity area in the room. Therefore, the larger monitoring range indicates we need to deploy more RFID antennas to cover all the monitoring area. 2) Based on our sensing model, the ambient environment around the tag array is supposed to be relatively stable, so that the signal interference can be well canceled to extract the reflection signal. Therefore, the frequent and large activities may unfortunately distort the ambient environment and lead to large errors of HRV estimation. To

[1]The tag is first sticking on the silicone gel sheet, and then sticking them all on the chest.

handle the unavoidable activities in daily life, we can segment the signals according to the large activities and focus on the periods without the large activities to estimate the HRV information. For example, we can monitor the users when they are sleeping or sitting for resting.

Comparison with wearable devices. Wearable sensors (*e.g.*, wrist band or belt) have brought great convenience in the perception of heart rate, especially when the user is performing exercises. Currently, the wearable devices usually only provide coarse-grained heart rate estimation over a period of time, which is a helpful metric for efficient exercising and training. In contrast, RF-ECG is designed to monitor the heart beat like the traditional ECG through a wireless manner in a relative stationary environment, and the user is supposed to sit quietly or sleep. Hence, RF-ECG can achieve the *fine-grained* IBI information from the stationary environment. But the user need to deploy different RFID devices to extend the monitoring scope, *e.g.*, one antenna for sleep monitoring in the bedroom and another antenna for daily monitoring in the living room. However, when RF-ECG need to monitor multiple users, we can easily deploy multiple tag arrays on different people, which may only cost about one dollar based on the cheap passive RFID tags. Therefore, RF-ECG is more suitable for the stationary monitoring, especially monitoring at a certain place, and is more easier to extend to multiple users.

Future Work. Currently, RF-ECG is designed to estimate the fine-grained IBI values in the stationary environments, which is an interesting attempt to estimate the heart beat interval based on COTS devices. In the future, we will keep improving the performance of RF-ECG by extending the application from two aspects. On one hand, we will try to improve the accuracy of IBI estimation, so that RF-ECG can provide more efficient and accurate information for the treatment of heart problem. On the other hand, we will try to improve the robustness of RF-ECG, so that RF-ECG can provide the IBI estimation when the user is doing different kinds of activities.

7 CONCLUSION

In this paper, we propose RF-ECG that leverages a COTS RFID tag array to extract the detailed Inter-Beat Interval (IBI) for the Heart Rate Variability (HRV) analysis. The users only need to wear the clothes with the RFID tag array attached in the chest area. In particular, we develop a mechanism to eliminate the respiration signal by capturing the RF-signal variation of the tag array caused by the moving effect associated with respiration. Further, we build a reflection model to depict the relationship between the RF-signal variation from the tag array and the reflection effect from the heart beat. By leveraging the reflection model, we are able to fuse multiple reflection signals from the tag array for accurate estimation of HRV. We implement our RF-ECG system and examine it with 15 volunteers. Experiment results show that RF-ECG can achieve a median IBI error of $24ms$, which is a strong evidence of the feasibility and effectiveness of RF-ECG. Our approach demonstrates a low-cost and convenient solution to provide accurate Heart Rate Variability assessment via RFID tags.

ACKNOWLEDGMENTS

This work is partially supported by National Natural Science Foundation of China under Grant Nos. 61472185, 61321491, 61502224, 61702257; JiangSu Natural Science Foundation, No. BK20151390, BK20170648. This work is partially supported by Collaborative Innovation Center of Novel Software Technology and Industrialization. This work is partially supported by the program A for Outstanding PhD candidate of Nanjing University. This work is partially supported by the US National Science Foundation Grants CNS-1826647, CNS-1820624 and Army Office Research Grant W911NF-17-1-0467.

REFERENCES

[1] 2010. Sleep apnea: What is sleep apnea? *NHLBI: Health Information for the Public. U.S. Department of Health and Human Services* (2010).
[2] 2016. Cardiovascular disease. http://www.who.int/cardiovascular_diseases/global-hearts/Global_hearts_initiative/en/.
[3] 2016. Fitbit. http://www.fitbit.com/.
[4] 2016. Jawbone Up. https://jawbone.com/up.

[5] 2016. Polar. https://www.polar.com.
[6] 2017. ECG. https://en.wikipedia.org/wiki/Electrocardiography.
[7] 2017. HRV. https://en.wikipedia.org/wiki/Heart_rate_variability.
[8] 2017. PPG. https://en.wikipedia.org/wiki/Photoplethysmogram.
[9] Fadel Adib, Zachary Kabelac, and Dina Katabi. 2015. Multi-person motion tracking via RF body reflections. In *Proc. of USENIX NSDI*.
[10] Fadel Adib, Hongzi Mao, Zachary Kabelac, Dina Katabi, and Robert C Miller. 2015. Smart homes that monitor breathing and heart rate. In *Proceedings of the 33rd Annual ACM Conference on Human Factors in Computing Systems*. ACM, 837–846.
[11] Sena Agezo, Yuxiang Zhang, Ziyu Ye, Somesh Chopra, Shrenik Vora, and Timothy Kurzweg. 2016. Battery-free RFID heart rate monitoring system. In *Proceedings of IEEE Wireless Health (WH)*. IEEE.
[12] Rita Brugarolas, Tahmid Latif, James Dieffenderfer, Katherine Walker, Sherrie Yuschak, Barbara L Sherman, David L Roberts, and Alper Bozkurt. 2016. Wearable heart rate sensor systems for wireless canine health monitoring. *IEEE Sensors Journal* 16, 10 (2016), 3454–3464.
[13] Oscar Delgado-Mohatar, Amparo Fúster-Sabater, and Jose M. Sierra. 2011. A light-weight authentication scheme for wireless sensor networks. *Ad Hoc Networks* 9, 5 (2011), 727–735.
[14] Han Ding, Chen Qian, Jinsong Han, Ge Wang, Zhiping Jiang, Jizhong Zhao, and Wei Xi. 2016. Device-free detection of approach and departure behaviors using backscatter communication. In *Proceedings of the 2016 ACM International Joint Conference on Pervasive and Ubiquitous Computing*. ACM, 167–177.
[15] Han Ding, Longfei Shangguan, Zheng Yang, Jinsong Han, Zimu Zhou, Panlong Yang, Wei Xi, and Jizhong Zhao. 2015. Femo: A platform for free-weight exercise monitoring with rfids. In *Proc. of ACM SenSys*.
[16] Daniel M Dobkin. 2012. *The rf in RFID: uhf RFID in practice*. Newnes.
[17] Amy D Droitcour, Olga Boric-Lubecke, and Gregory TA Kovacs. 2009. Signal-to-noise ratio in Doppler radar system for heart and respiratory rate measurements. *IEEE transactions on microwave theory and techniques* 57, 10 (2009), 2498–2507.
[18] Hayato Fukushima, Haruki Kawanaka, Md Shoaib Bhuiyan, and Koji Oguri. 2012. Estimating heart rate using wrist-type photoplethysmography and acceleration sensor while running. In *Proceedings of Engineering in Medicine and Biology Society (EMBC)*. IEEE, 2901–2904.
[19] Mathew J Gregoski, Martina Mueller, Alexey Vertegel, Aleksey Shaporev, Brenda B Jackson, Ronja M Frenzel, Sara M Sprehn, and Frank A Treiber. 2012. Development and validation of a smartphone heart rate acquisition application for health promotion and wellness telehealth applications. *International journal of telemedicine and applications* 2012 (2012), 1.
[20] Mohinder S Grewal. 2011. *Kalman filtering*. Springer.
[21] G.S.Chung, B.H.Choi, K.K.Kim, Y.G.Lim, J.W. Choi, D.-U. Jeong, and K. S. Park. 2007. Rem sleep classification with respiration rates. In *Proc. of 6th IEEE ITAB*.
[22] Zhenhua Jia, Musaab Alaziz, Xiang Chi, Richard E Howard, Yanyong Zhang, Pei Zhang, Wade Trappe, Anand Sivasubramaniam, and Ning An. 2016. HB-phone: a bed-mounted geophone-based heartbeat monitoring system. In *15th ACM/IEEE International Conference on Information Processing in Sensor Networks (IPSN)*. IEEE.
[23] Kiran Raj Joshi, Dinesh Bharadia, Manikanta Kotaru, and Sachin Katti. 2015. WiDeo: Fine-grained Device-free Motion Tracing using RF Backscatter.. In *NSDI*. 189–204.
[24] Ricardo Belchior Lagido, Joana Lobo, S Leite, C Sousa, Liliana Ferreira, and J Silva-Cardoso. 2014. Using the smartphone camera to monitor heart rate and rhythm in heart failure patients. In *Biomedical and Health Informatics (BHI), 2014 IEEE-EMBS International Conference on*. IEEE, 556–559.
[25] Jia Liu, Min Chen, Shigang Chen, Qingfeng Pan, and Lijun Chen. 2017. Tag-Compass: Determining the Spatial Direction of an Object with Small Dimensions. In *Proc. of IEEE INFOCOM*. 1–9.
[26] Jian Liu, Yan Wang, Yingying Chen, Jie Yang, Xu Chen, and Jerry Cheng. 2015. Tracking vital signs during sleep leveraging off-the-shelf wifi. In *Proceedings of the 16th ACM International Symposium on Mobile Ad Hoc Networking and Computing*. ACM, 267–276.
[27] Jia Liu, Feng Zhu, Yanyan Wang, Xia Wang, Qingfeng Pan, and Lijun Chen. 2017. RF-Scanner: Shelf scanning with robot-assisted RFID systems. In *Proc. of IEEE INFOCOM*. 1–9.
[28] Xuefeng Liu, Jiannong Cao, Shaojie Tang, Jiaqi Wen, and Peng Guo. 2016. Contactless Respiration Monitoring Via Off-the-Shelf WiFi Devices. *IEEE Transactions on Mobile Computing* 15, 10 (2016), 2466–2479.
[29] Wansuree Massagram, Victor M Lubecke, Anders HØst-Madsen, and Olga Boric-Lubecke. 2009. Assessment of heart rate variability and respiratory sinus arrhythmia via Doppler radar. *IEEE Transactions on Microwave Theory and Techniques* 57, 10 (2009), 2542–2549.
[30] Phuc Nguyen, Xinyu Zhang, Ann Halbower, and Tam Vu. 2016. Continuous and fine-grained breathing volume monitoring from afar using wireless signals. In *The 35th Annual IEEE International Conference on Computer Communications, IEEE INFOCOM*. IEEE.
[31] Panagiotis Pelegris, K Banitsas, T Orbach, and Kostas Marias. 2010. A novel method to detect heart beat rate using a mobile phone. In *Engineering in Medicine and Biology Society (EMBC), 2010 Annual International Conference of the IEEE*. IEEE, 5488–5491.
[32] Mark Roberti. 2004. EPCglobal ratifies Gen 2 standard. *RFID Journal* 16 (2004).
[33] Sylvain Sardy, Paul Tseng, and Andrew Bruce. 2001. Robust wavelet denoising. *IEEE Transactions on Signal Processing* 49, 6 (2001), 1146–1152.

[34] Longfei Shangguan and Kyle Jamieson. 2016. Leveraging Electromagnetic Polarization in a Two-Antenna Whiteboard in the Air. In *Proceedings of the 12th International on Conference on emerging Networking EXperiments and Technologies*. ACM, 443–456.
[35] Harald M Stauss. 2003. Heart rate variability. *American Journal of Physiology-Regulatory, Integrative and Comparative Physiology* 285, 5 (2003), R927–R931.
[36] Hao Wang, Daqing Zhang, Junyi Ma, Yasha Wang, Yuxiang Wang, Dan Wu, Tao Gu, and Bing Xie. 2016. Human respiration detection with commodity wifi devices: do user location and body orientation matter?. In *Proceedings of the 2016 ACM International Joint Conference on Pervasive and Ubiquitous Computing*. ACM, 25–36.
[37] Jue Wang, Deepak Vasisht, and Dina Katabi. 2015. RF-IDraw: virtual touch screen in the air using RF signals. In *Proc. of ACM SIGCOMM*.
[38] Teng Wei and Xinyu Zhang. 2016. Gyro in the air: tracking 3D orientation of batteryless internet-of-things. In *Proc. of ACM Mobicom*. 55–68.
[39] Yaxiong Xie, Zhenjiang Li, and Mo Li. 2015. Precise power delay profiling with commodity wifi. In *Proceedings of the 21st Annual International Conference on Mobile Computing and Networking*. ACM.
[40] Lei Yang, Yekui Chen, Xiang-Yang Li, Chaowei Xiao, Mo Li, and Yunhao Liu. 2014. Tagoram: Real-time tracking of mobile RFID tags to high precision using COTS devices. In *Proc. of ACM MobiCom*.
[41] Lei Yang, Qiongzheng Lin, Xiangyang Li, Tianci Liu, and Yunhao Liu. 2015. See through walls with cots rfid system!. In *Proceedings of the 21st Annual International Conference on Mobile Computing and Networking*. ACM, 487–499.
[42] Mingmin Zhao, Fadel Adib, and Dina Katabi. 2016. Emotion recognition using wireless signals. In *Proceedings of the 22nd Annual International Conference on Mobile Computing and Networking*. ACM, 95–108.
[43] Liang Zou, Xun Chen, Amir Servati, Saeid Soltanian, Peyman Servati, and Z Jane Wang. 2016. A Blind Source Separation Framework for Monitoring Heart Beat Rate Using Nanofiber-Based Strain Sensors. *IEEE Sensors Journal* 16, 3 (2016), 762–772.

Received August 2017; revised February 2018; accepted June 2018